View Online / Journal Homepage
Dynamic Article Links

Journal of
Materials Chemistry

Cite this: DOI: 10.1039/c2jm30221g

www.rsc.org/materials

PAPER

Fabrication and electrochemical performances of hierarchical porous $Ni(OH)_2$ nanoflakes anchored on graphene sheets†

Jun Yan,[a] Wei Sun,[a] Tong Wei,[a] Qiang Zhang,[b] Zhuangjun Fan*[a] and Fei Wei[b]

Received 12th January 2012, Accepted 13th March 2012
DOI: 10.1039/c2jm30221g

Hierarchical porous $Ni(OH)_2$ nanoflakes anchored on graphene sheets has been fabricated by a facile chemical precipitation approach. The as-prepared $Ni(OH)_2$/graphene composite as a electrode material for supercapacitors displays ultrahigh specific capacitance, superior cycling performance, and excellent rate capability. A maximum specific capacitance of 2194 F g^{-1} could be obtained at 2 mV s^{-1} in 6 M KOH aqueous solution. Meanwhile, the electrode exhibits excellent long cycle life along with 95.7% specific capacitance retained after 2000 cycle tests. Such composite is a highly promising candidate as electrode material for broad applications in energy conversion/storage systems.

1. Introduction

Recently, the increasing power demands for electric vehicles and power tools have forced scientists and researchers to exploit highly effective devices to store electrical energy. Supercapacitors, also called electrochemical capacitors or ultracapacitors, have attracted considerable attention as novel energy storage devices by virtue of their high power density, long cycling life, short charging time and environmental benignity, which make them highly promising for critical applications, such as low- or zero-emission hybrid electrical and electrical vehicles, energy-efficient cargo ships and locomotives, aerospace and power-grid applications.[1–3] Based on different charge storage mechanisms, supercapacitors can be classified into electrical double-layer capacitors (EDLC) or pseudocapacitors. The former utilizes the capacitance arising from charge separation at the electrode/electrolyte interface, while the latter is based on the fast and reversible faradic redox reaction of electroactive materials.[4] Generally, pseudocapacitors show remarkably larger capacitance than the EDLC. Transition metal oxides and conducting polymers are commonly used as electrode materials for pseudocapacitors.[1,5] Among them, RuO_2 has been recognized as the ideal electrode material due to its ultrahigh pseudocapacitance (~1300 F g^{-1}) and excellent reversibility.[1,6] However, the expensive nature significantly limits their actual application on a large scale for commercialization.[4] Therefore, the development of alternative inexpensive materials with excellent capacitive performances similar to RuO_2 is of great technological importance for critical applications.

Nickel hydroxide as one of the most promising candidates has received tremendous attention in recent years due to the low cost, high theoretical capacitance (2082 F g^{-1} within 0.5 V), ready availability, environmentally benign nature and high stability in alkaline electrolyte.[7] However, there is still a great challenge associated with the use of high-capacity $Ni(OH)_2$ electrodes. The poor electrical conductivity and the large volume change, commonly occurring during the charge/discharge process, greatly restrict its practical application. Hence, it is crucial to improve the electrical conductivity and increase the rate capability and capacitance retention to further enhance the energy and power densities. In order to overcome this problem, recently numerous effort has been focus on improving the performance of the electrode, such as enhancing the stability of the α-$Ni(OH)_2$,[8] using additives,[9,10] surface modification [11] and synthesis of nanoscale materials.[12,13] Among these strategies, it has been demonstrated that introducing various highly electrically conductive carbonaceous materials into $Ni(OH)_2$ to prepare composites is an effective and promising approach. Such conductive carbonaceous materials mainly include activated carbon,[14] carbon nanotube,[15] mesoporous carbon[16] and graphene.[17] Graphene, emerging as a new two-dimensional material with atomic thickness, has now aroused tremendous attention of scientists worldwide due to its high surface area (~2600 m^2 g^{-1}), low cost, high electrical conductivity (10^3–10^4 S m^{-1}), excellent chemical stability and superior mechanical, thermal and electrical properties.[18] It is these characteristics that hold great promise for potential applications in energy storage field.[19] However, graphene-based nanomaterials generally possess unsatisfactory specific capacitance as high as 100–200 F g^{-1}, which can be attributed to the poor utilization of the intrinsic high surface area due to the irreversible agglomeration/

---

[a] *Key Laboratory of Superlight Materials and Surface Technology, Ministry of Education, College of Material Science and Chemical Engineering, Harbin Engineering University, Harbin 150001, China. E-mail: fanzhj666@163.com; Tel: +86 451 82569890*
[b] *Beijing Key Laboratory of Green Chemical Reaction Engineering and Technology, Department of Chemical Engineering, Tsinghua University, Beijing 100084, China*

† Electronic supplementary information (ESI) available. See DOI: 10.1039/c2jm30221g

restacking of graphene sheets during the preparation or drying process.[20] In order to avoid the shortcomings of single material and to obtain promising materials with both high capacitance performance and good cycle life, chemists and material scientists are striving to explore synergistic composite materials around the world. Therefore, from the material science point of view, it is highly expected to achieve outstanding performances in terms of ultrahigh specific capacitance, excellent high-rate capability and superior cycling stability through rational structure design to incorporate highly conductive graphene sheets with low-cost pseudocapacitive $Ni(OH)_2$ material, which could take full advantage of the positive synergistic effects between graphene sheets and $Ni(OH)_2$. The graphene sheets in the composite could not only provide a support with high specific surface for the deposition of nanometer-sized $Ni(OH)_2$ particles, resulting in high electrochemical utilization of $Ni(OH)_2$, but also efficiently buffer the volume expansion/contraction during the rapid charge/discharge process. In addition, the $Ni(OH)_2$ nanoparticles anchored on graphene sheets may act as a spacer to effectively prevent the restacking of graphene sheets and consequently maintain the high surface area.

In this paper, we report a facile approach to fabricate hierarchical porous $Ni(OH)_2$ nanoflakes decorated on graphene sheets through *in situ* chemical precipitation. It is demonstrated that the $Ni(OH)_2$/graphene sheets composite has the advantages of the two building blocks and exhibits a large reversible capacitance, enhanced cyclic stability and excellent rate capability.

2. Experimental

Synthesis of $Ni(OH)_2$/graphene composites

Graphene sheets were prepared by chemical reduction of graphene oxide with hydrazine hydrate according to the previous literature.[21] $Ni(OH)_2$/graphene composites were synthesized by a facile chemical precipitation method without any hard/soft templates as follows (Fig. 1): Typically, 0.2 g of graphene sheets were added into 210 mL of distilled water and subjected to ultrasonication for 30 min. Then 5 g of nickel chloride hexahydrate was added into above suspension and stirred for 30 min. Subsequently, 5% ammonia hydroxide solution was added into the suspension drop by drop until the pH 9.5 under vigorous stirring. Finally, the black precipitate was obtained by filtration, washed several times with ethanol and distilled water, and dried in an oven at 100 °C for 12 h. For comparison, pure $Ni(OH)_2$ was also prepared according to the same method as described above in the absence of graphene sheets. The mass fraction of $Ni(OH)_2$ grown on graphene was 80 wt.%, which was obtained by comparing the mass of the prepared composite with the mass of pristine graphene used in the synthesis.

Characterization methods

The crystallographic structures of the materials were determined by a powder X-ray diffraction system (XRD, TTR-III) equipped with Cu-Kα radiation ($\lambda = 0.15406$ nm). Transmission electron microscopy (TEM) characterizations were carried out using a transmission electron microscope (JEOL JEM2010). X-ray energy dispersive spectroscopy (EDX) was performed on a field-emission scanning electron microscope (FESEM, Hitachi S4800). X-ray photoelectron spectroscopy (XPS) measurements were performed using a PHI 5700 ESCA spectrometer with a monochromated Al Kα radiation ($h\nu = 1486.6$ eV). Raman spectra were obtained on a Renishaw RM2000 Raman spectrometer with 457.9 nm wavelength incident laser light. The N_2 adsorption-desorption isotherms of the samples were measured at 77 K using Micrometrics Flowsorb II 2300 (Micromeritics, USA). The specific surface area was calculated from the Brunauer–Emmett–Teller (BET) plot of the nitrogen adsorption isotherm and the pore size distribution of the samples was calculated from adsorption branch isotherms by Barrett–Joyner–Halenda (BJH) method.

Preparation of electrodes and electrochemical measurement

The fabrication of working electrodes was carried out as follows: Briefly, the as-prepared materials, carbon black and poly(tetrafluoroethylene) were mixed in a mass ratio of 75 : 20 : 5 and dispersed in ethanol. Then the resulting slurry was coated onto the nickel foam substrate (1 cm × 1 cm) with a spatula, and followed by drying at 100 °C for 12 h in a vacuum oven.

All electrochemical measurements were done in a three-electrode setup: Ni foam coated with electroactive materials as the working electrode, platinum foil and saturated calomel electrode (SCE) as the counter and reference electrodes. The measurements were carried out in a 6 M KOH aqueous electrolyte at room temperature. Cyclic voltammograms (CV) and electrochemical impedance spectroscopy (EIS) were measured by a CHI 660C electrochemical workstation. CV tests were done between −0.1 to 0.45 V (*vs.* SCE) at different scan rates. EIS measurements were carried out in the frequency range from 100 kHz to 0.1 Hz at open circuit potential with an ac perturbation of 5 mV. The specific capacitance of the electrode can be calculated from the CV curves according to the following equation:

$$C = (\int I\,\mathrm{d}V)/(\upsilon m V) \qquad (1)$$

where I is the response current density (A cm^{-2}), V is the potential (V), υ is the potential scan rate (V s^{-1}), and m is the mass of the electroactive materials in the electrodes (g cm^{-2}).

3. Results and discussion

Microstructure characterizations

Fig. 2a shows the XRD profile of as prepared $Ni(OH)_2$/graphene composite, together with the pristine graphene sheets and $Ni(OH)_2$ nanoplates for comparison. Two diffraction peaks for pristine graphene sheets appears at around $2\theta = 24.06°$ and 43.1°, corresponding to the (002) and (101) reflections of graphene sheets, respectively. The interlayer spacing calculated from the Bragg equation is about 0.37 nm, which is slightly higher than that of well ordered graphite (0.34 nm), suggesting the presence of some residual oxygen functionalities on the graphene sheets due to the incomplete reduction by hydrazine hydrate. The broad nature of the reflection peaks implies increased disorder of the sheets in the through-plane direction, demonstrating that the samples are composed of mostly single or few layers of graphene sheets.[22,23] The diffraction pattern of pure $Ni(OH)_2$ sample exhibits a set of characteristic diffraction peaks, and all of them can be unambiguously indexed to the pure hexagonal phase of

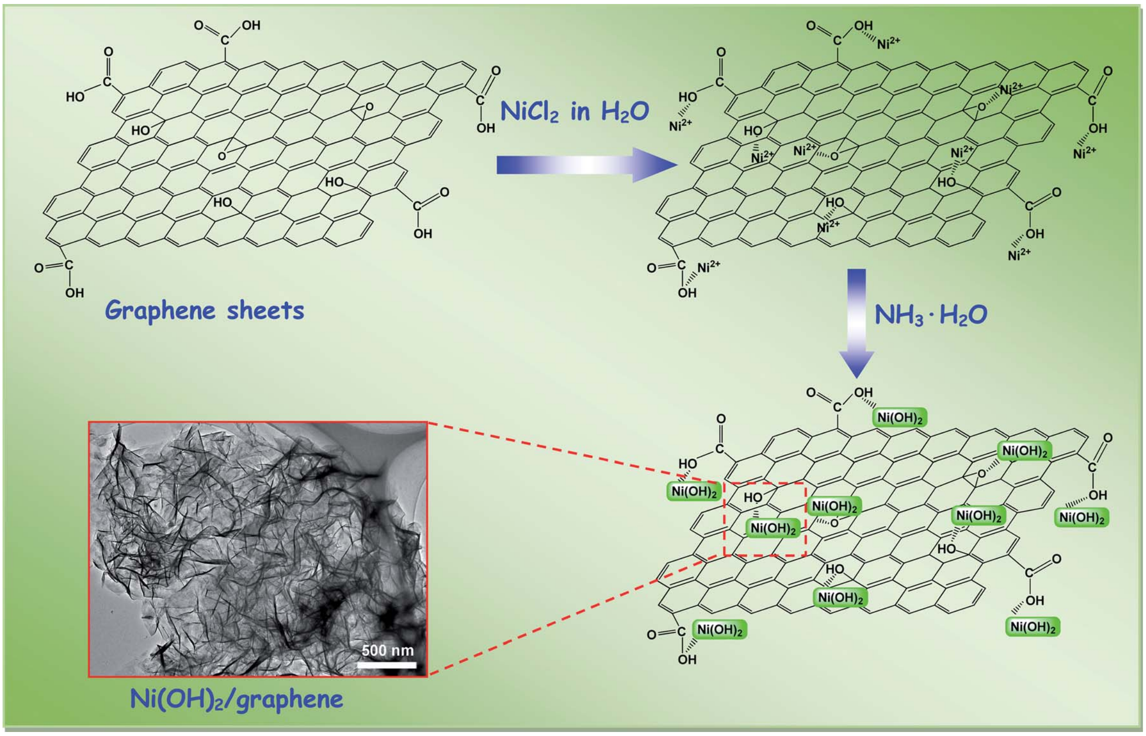

Fig. 1 Schematic illustration of the synthesis route towards the $Ni(OH)_2$/graphene composite.

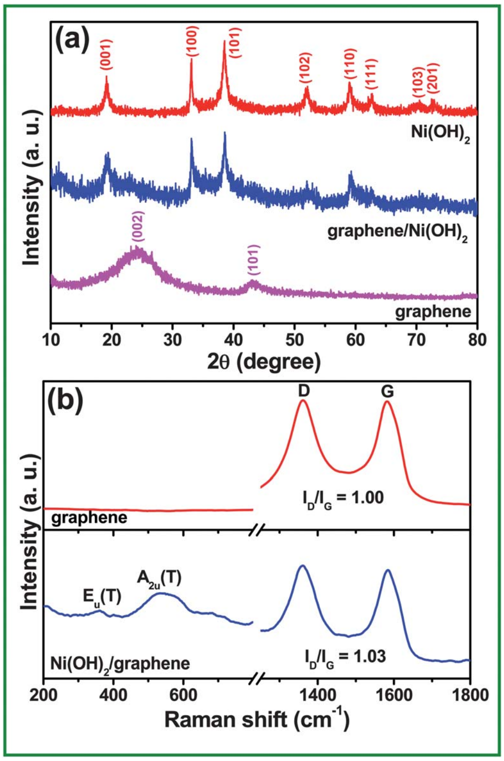

Fig. 2 (a) Typical XRD patterns of the pristine graphene sheets, $Ni(OH)_2$ nanoplates and the as-prepared $Ni(OH)_2$/graphene composite. (b) Raman spectra of the pristine graphene sheets and $Ni(OH)_2$/graphene composite.

β-$Ni(OH)_2$ with lattice parameters of $a = b = 0.3126$ nm and $c = 0.4606$ nm (JCPDS card no. 14-0117, the space group: P-3m1(164)), which is in good agreement with the reported pattern for β-$Ni(OH)_2$.[24] It is worth noting that the (100) and (101) diffraction peaks are more sharp than other peaks, indicating the plate-like shape of β-$Ni(OH)_2$. In addition, the XRD pattern of the $Ni(OH)_2$/graphene composite is similar to that of pure $Ni(OH)_2$, meaning that $Ni(OH)_2$ with high purity can be well synthesized on the graphene sheets. Remarkably, the characteristic diffraction peaks of graphene sheets have disappeared in the XRD pattern of $Ni(OH)_2$/graphene composite owing to more disordered stacking and quite uniform dispersion of graphene sheets in the resulting composite.

The Raman spectra of pristine graphene sheets and the $Ni(OH)_2$/graphene composite are shown in Fig. 2b. Both of the two curves exhibit two prominent peaks at 1362 and 1583 cm^{-1}, corresponding to the D and G bands of graphene, respectively. Generally, in the Raman spectrum, the G band represents the in-plane bond-stretching motion of the pairs of C sp^2 atoms (the E_{2g} phonons); while the D band corresponds to the breathing modes of rings or κ-point phonons of A_{1g} symmetry.[21] Commonly, the peak intensity ratio of the D and G band (I_D/I_G) can be used to roughly estimate the disorder degree and average size of the sp^2 domains of the graphite materials. Compared to pristine graphene sheets, the I_D/I_G ratio of the $Ni(OH)_2$/graphene composite is slightly increased from 1.00 to 1.03, which is perhaps due to the decrease in the size of the sp^2 graphitic domains during the preparation process and the presence of some unrepaired defects.[25] In addition, it could be observed that two additional Raman modes center at 361 and 532 cm^{-1}, which can be identified to the E_u(T) and A_{2u}(T) lattice vibrations of $Ni(OH)_2$,

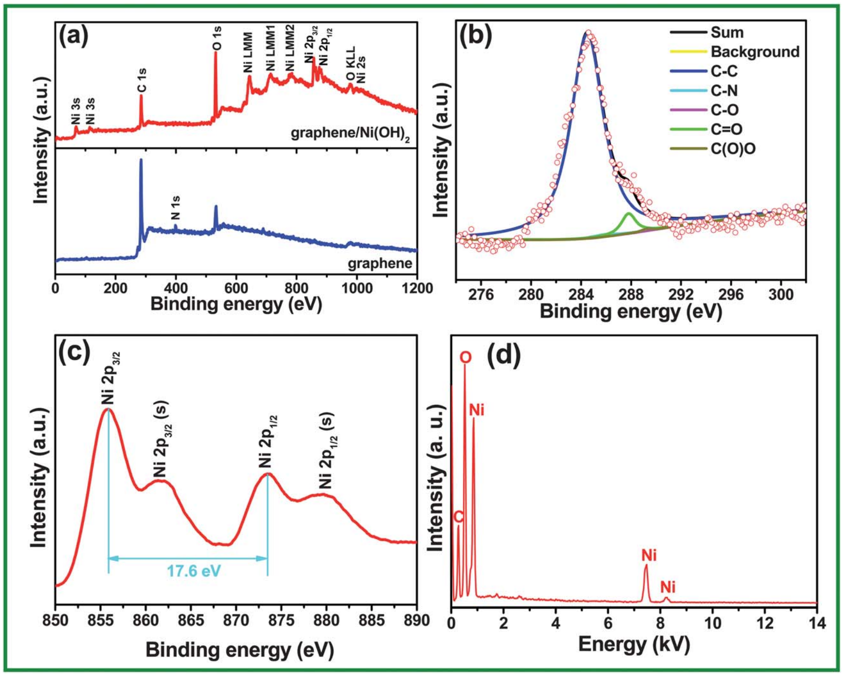

Fig. 3 XPS spectra of the pure $Ni(OH)_2$ and as-prepared $Ni(OH)_2$/graphene composite. (a) XPS survey spectra. (b) C 1s spectrum and (c) Ni 2p spectrum of the $Ni(OH)_2$/graphene composite. (d) EDX characterization of the $Ni(OH)_2$/graphene composite.

respectively.[26] These results further confirm that $Ni(OH)_2$ has been successfully anchored on the graphene sheets.

In order to further confirm the XRD and Raman results, important information on the surface electronic state and the composition of the $Ni(OH)_2$/graphene composite were examined by XPS measurements (Fig. 3). Compared to the pristine graphene sheets, the survey spectrum of the $Ni(OH)_2$/graphene composite mainly shows carbon, oxygen and nickel species. The peak located at 284.6 eV is ascribed to the characteristic peak of C 1s, which can be divided into several peaks (Fig. 3b), indicating that there are still some residual oxygen-containing functionalities on the graphene sheets due to the incomplete reduction. In addition, the Ni 2p XPS spectrum shows two major peaks centered around 873.5 and 855.9 eV with a spin-energy separation of 17.6 eV (Fig. 3c), corresponding to Ni $2p_{1/2}$ and Ni $2p_{3/2}$, respectively, which is the characteristic of a $Ni(OH)_2$ phase and in good agreement with the previous literature.[27] This result is also consistent with the XRD and Raman analysis as mentioned above. Remarkably, there are some extra peaks labeled as satellite peaks present around the expected Ni $2p_{1/2}$ and Ni $2p_{3/2}$ signals in the Ni 2p region as shown in Fig. 3c. EDX characterization reveals that the composite is primarily composed of Ni, C and O (Fig. 3d). Based on the element analysis result, the content of graphene is about 21.8% in the composite, which is in good agreement with the result calculated from the mass difference between before and after the deposition.

Fig. 4 shows the TEM images of pure $Ni(OH)_2$ nanoplate and as-prepared $Ni(OH)_2$/graphene composite. It can be seen that the pure $Ni(OH)_2$ nanosheets have a typical size in the range from several tens to several hundreds of nanometer with obvious microscopic roughening instead of perfectly flat sheets (Fig. 4a). These nanosheets interconnect with each other to randomly form big disordered aggregations with crumpled sheets closely associated with each other. After the incorporation of graphene sheets (Fig. 4b and c), the smaller and thinner $Ni(OH)_2$ nanosheets homogeneously distribute on graphene sheets with a lateral dimension of ~300 nm and ~3 nm in thickness compared to pure $Ni(OH)_2$ nanosheets. Interestingly, numerous mesopores (~2 nm) can be observed on the $Ni(OH)_2$ nanosheet as indicated by arrows (Fig. 4d), which is favorable for the rapid transport/diffusion of electrolyte ions during the redox reaction,[28] ensuring the sufficient Faradaic reaction taking place at high current densities and accordingly excellent high-rate

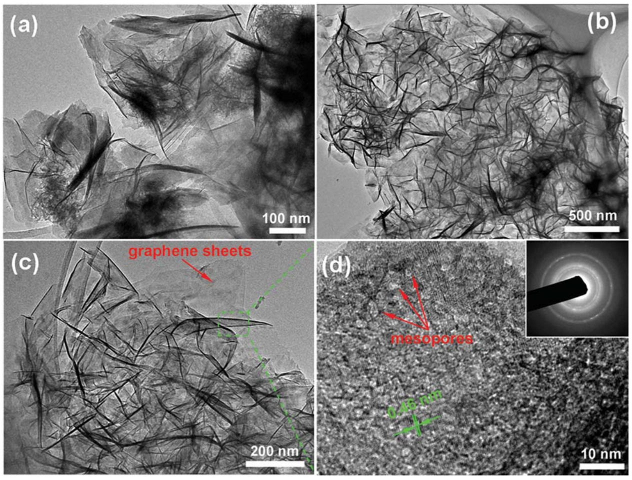

Fig. 4 (a) TEM image of pure $Ni(OH)_2$ nanoplates. (b, c) TEM images of $Ni(OH)_2$/graphene composite. (d) High resolution TEM image of the square region in Fig. 4c, inset is the corresponding SAED pattern.

capability. In addition, the measured lattice spacing of about 0.46 nm is well consistent with the interplanar spacing of the (001) crystal plane of the β-$Ni(OH)_2$ phase (Fig. 4d). Furthermore, the corresponding selected area electronic diffraction (SAED) pattern shows a set of concentric diffuse rings revealing the existence of $Ni(OH)_2$ phase with a polycrystalline nature (inset of Fig. 4d).

The nitrogen adsorption/desorption isotherms of the prepared pristine $Ni(OH)_2$ and graphene/$Ni(OH)_2$ samples at 77 K and the corresponding pore size distribution are shown in Fig. 5. The isotherms of both pristine $Ni(OH)_2$ and graphene/$Ni(OH)_2$ composite can be identified as type IV according to the IUPC classification, which is characteristic of mesoporous materials.[13] A obvious hysteresis loop could be observed in the range of 0.4–0.9 P/P_0, suggesting the presence of mesopores. The graphene/$Ni(OH)_2$ composite exhibits a BET surface area of 220 $m^2\ g^{-1}$, which is slightly higher than that of the pristine $Ni(OH)_2$ sample (218 $m^2\ g^{-1}$). The pore size distribution calculated from the desorption branch using the BJH modal of the graphene/$Ni(OH)_2$ composite seem very similar to that of pristine $Ni(OH)_2$ sample and shows the mean pore size of ~2 nm (Fig. 5b), which is in accordance with the TEM observation (Fig. 4d). In addition, some mesopores/macropores in the range of 3–60 nm can also be observed, which could be attributed to the interleaving structures of the $Ni(OH)_2$ nanosheets. These considerable mesopores and macropores can facilitate the rapid transport and migration of electrolyte ions during the charge/discharge process, which is highly desirable for high-rate supercapacitors with high power densities.

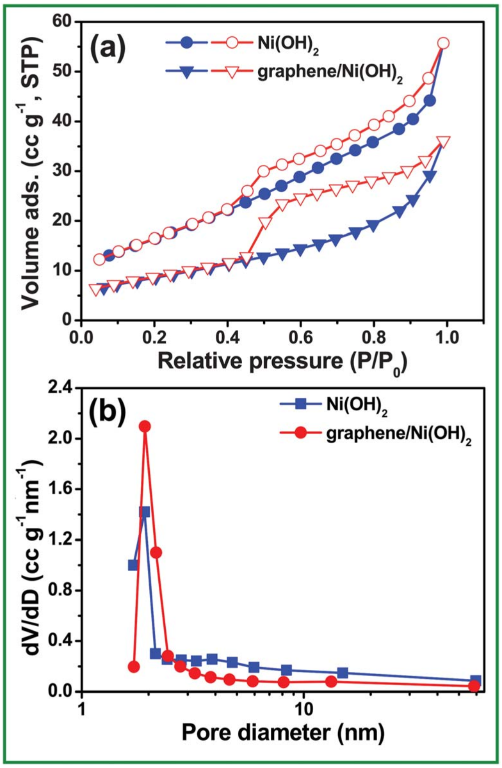

Fig. 5 (a) Nitrogen adsorption/desorption isotherms and (b) pore-size distribution curves for $Ni(OH)_2$ and graphene/$Ni(OH)_2$ nanostructures.

Electrochemical behaviour

CV is generally considered as a suitable tool to characterize the capacitive behaviour and quantify the specific capacitance of an electrode material. Fig. 6 shows the CV curves of pure $Ni(OH)_2$ and the $Ni(OH)_2$/graphene composite at different scan rates ranging from 2 to 40 mV s^{-1} within the potential window of −0.1 to 0.45 V (*vs.* SCE) in 6 M KOH solution. It is obvious that all of the CV curves exhibit two intense redox peaks, and the shapes of the CV curves are well distinguished from that of the EDLC, in which case it is normally close to an ideal rectangular shape, indicating that the specific capacitance primarily originates from the pseudocapacitive capacitance based on a redox mechanism. This is in accordance with the galvanostatic charge/discharge curves of the graphene/$Ni(OH)_2$ electrode as shown in Fig. S1 (ESI†). The anodic peak (positive current density) occurred around 0.30 V (*vs.* SCE) indicates an oxidation process due to the oxidation of $Ni(OH)_2$ to NiOOH, while the cathodic peak (negative current density) observed around 0.10 V (*vs.* SCE) corresponds to the reverse process. For $Ni(OH)_2$ electrode material, it is well-accepted that the surface Faradaic reactions will proceed according to the following reaction:[17]

$$Ni(OH)_2 + OH^- \rightleftharpoons NiOOH + H_2O + e \qquad (2)$$

The symmetric characteristic of anodic charges and cathodic charges reveals the excellent reversibility of the electrode due to the facile ion diffusion and good adsorption behaviour. It should also be noted that a slight positive shift of oxidation peaks and a negative shift of reduction peaks can be observed with an increase of scan rates, which is mainly due to the resistance of the electrode. In addition, the shape of the CV curves is not significantly influenced as the scan rates increase from 2 to 50 mV s^{-1}, which is resulted from the improved mass transportation and electron conduction within the material. Since the specific capacitance is proportional to the area surrounded by the CV curves, the area under the CV curves for the $Ni(OH)_2$/graphene composite is higher than that of pure $Ni(OH)_2$ electrode at the same scan rate, indicating the higher specific capacitance. This can be attributed to the enhanced electrical conductivity and facilitated ion transport and diffusion rate. In order to verify the above point, the effect of scan rates on the anodic peak currents of the two electrodes was also investigated as shown in Fig. 6c. It is noteworthy that the anodic current (I_p) increase linearly with the square root of the scan rate ($v^{1/2}$) at all scan rates (Fig. 6c), indicating that the redox reaction of $Ni(OH)_2$ in KOH solution is a diffusion-controlled process.[29,30]

Generally speaking, the peak current of diffusion controlled reversible electrochemical reaction follows Randles-Sevcik equation,[31] which assumes that mass transport occurs only by a diffusion process:

$$I_p = (2.69 \times 10^5)n^{3/2}\ ACD^{1/2}v^{1/2} \qquad (3)$$

where I_p is the peak current (A), n is the number of electrons transferred during the redox reaction, A is the effective surface area of the working electrode (cm^2), C is the concentration of the diffusing species in the bulk of the electrolyte (mol cm^{-3}), D is the

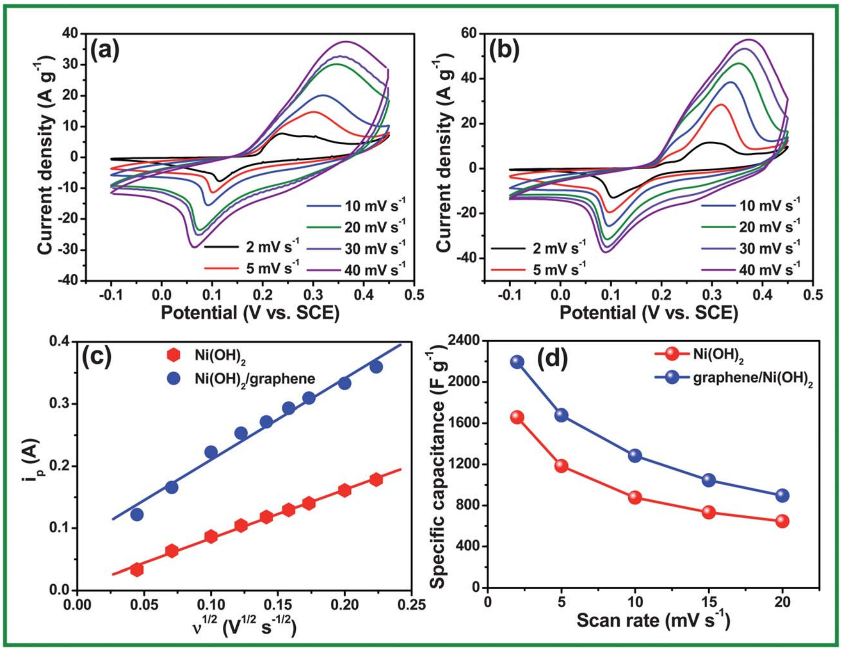

Fig. 6 CV curves of pure $Ni(OH)_2$ nanoplates (a) and $Ni(OH)_2$/graphene composite electrode (b) at different scan rates within a potential range of −0.1 to 0.45 V (*vs.* SCE) in 6 M KOH aqueous solution. (c) Relationship between anodic peak current and square root of scan rates for pure $Ni(OH)_2$ nanoplates and $Ni(OH)_2$/graphene composite electrode.

diffusion coefficient (cm^2 s^{-1}), ν is the potential scan rate (V s^{-1}). According to the above equation, the diffusion coefficient D is calculated to be 6.58×10^{-7} cm^2 s^{-1} for $Ni(OH)_2$/graphene composite electrode, which is nearly three times that of the pure $Ni(OH)_2$ electrode (2.38×10^{-7} cm^2 s^{-1}). In the composite, graphene sheets can provide high specific surface support for the nucleation of $Ni(OH)_2$ nanoparticles and enable the $Ni(OH)_2$ particles disperse homogeneously in nanometer size on the surface of graphene sheets, which effectively prevents the aggregation of the nanoparticles and accordingly significantly increases the contact area between $Ni(OH)_2$ nanoplates and electrolyte ions and shortens the ion diffusion/migration pathways. In addition, the numerous nanopores on the surfaces of $Ni(OH)_2$ nanoplates may provide electrolyte ions with facile diffusion channels and facilitate their transport and diffusion during rapid charge/discharge process. In consideration of this respect, the diffusion of the OH^- is enhanced compared to the pure $Ni(OH)_2$ nanoplate electrode, which is favorable for the improvement of the electrochemical performance as an electrode for supercapacitors.

Fig. 6d shows the specific capacitance of pure $Ni(OH)_2$ and $Ni(OH)_2$/graphene composite at different scan rates in 6 M KOH solution. Overall, the specific capacitance of both samples decreases with increasing scan rates, but the specific capacitance of the $Ni(OH)_2$/graphene composite is always higher than that of pure $Ni(OH)_2$ electrode at all scan rates. The specific capacitance of the $Ni(OH)_2$/graphene composite is calculated to be 2194 F g^{-1} at a scan rate of 2 mV s^{-1}, which is much higher than that of the pure $Ni(OH)_2$ electrode (1657 F g^{-1}) and graphene (183.6 F g^{-1}), suggesting that the specific capacitance predominantly stems from the redox pseudocapacitance of $Ni(OH)_2$. Notably, the specific capacitance of the composite is highly comparable to those of the previously reported data in literature for $Ni(OH)_2$ based materials (see Table 1), which is most probably due to the nano-size of $Ni(OH)_2$ particles and high electrical conductivity of the composite, resulting in high electrochemical utilization of the active material. Even at 20 mV s^{-1}, the specific capacitance of the $Ni(OH)_2$/graphene composite can be kept as high as 895 F g^{-1}, indicating that the composite has a good rate capability which is quite crucial for the electrode materials of supercapacitors to achieve both high power and energy densities.

EIS provides complementary information about the frequency response of electrode materials in supercapacitors and allows us to estimate the capacitance changes with the operating frequency.[32,33] It is well known that the complex form of capacitance is dependent on frequency, which is defined as follows:[34,35]

$$C(\omega) = C'(\omega) - jC''(\omega) \tag{4}$$

where $C'(\omega)$ and $C''(\omega)$ are the real part and imaginary part of the complex capacitance $C(\omega)$, respectively, and they are expressed as formulas 5 and 6:[34,35]

$$C'(\omega) = \frac{-Z''(\omega)}{\omega|Z(\omega)|^2} \tag{5}$$

$$C''(\omega) = \frac{-Z'(\omega)}{\omega|Z(\omega)|^2} \tag{6}$$

where $Z'(\omega)$ and $Z''(\omega)$ are the respective real and imaginary parts of the complex impedance $Z(\omega)$. ω is the angular frequency which is given by $\omega = 2\pi f$. At low frequency, $C'(\omega)$ corresponds to the capacitance of the electrode material and $C''(\omega)$ is ascribed to the energy dissipation by an irreversible process that leads to a hysteresis.[34,35] Fig. 7 shows the normalized real and imaginary

Table 1 Summary of electrochemical data of $Ni(OH)_2$ based electrodes. Complete data can be found in the related literature

Sample	Technique	Specific capacitance (F g^{-1})	Electrolyte	Potential window (V)	Current load or scan rate	Ref.
α-$Ni(OH)_2$	Hydrothermal	1715	1 M KOH	0.60	5 mV s^{-1}	13
α-$Ni(OH)_2$	Precipitation	805	1 M KOH	0.55	5 mV s^{-1}	42
α-$Ni(OH)_2$	Chemical precipitation	1328	1 M KOH	0.45	1 A g^{-1}	43
α-$Ni(OH)_2$	Converse migration	833	6 M KOH	0.54	5 mA cm^{-2}	44
α-$Ni(OH)_2$	Chemical precipitation	2222	1 M KOH	0.50	1 A g^{-1}	37
β-$Ni(OH)_2$	Cathodic electrodeposition	1056	1 M KOH	0.55	2 mV s^{-1}	45
β-$Ni(OH)_2$	Hydrothermal	2675	1 M NaOH	0.55	5 mA cm^{-2}	46
β-$Ni(OH)_2$	Cathodic electrodeposition	897	1 M KOH	0.55	2 A g^{-1}	47
β-$Ni(OH)_2$	Chemical precipitation	398	2 M KOH	0.50	5 mV s^{-1}	48
$Ni(OH)_2$/ZnO	Hydrothermal	1310	1 M NaOH	0.55	15.7 A g^{-1}	49
$Ni(OH)_2$/CMK-3	Chemical precipitation	2570	2 M KOH	0.40	0.625 A g^{-1}	16
$Ni(OH)_2$/CNTs	Hydrothermal	1303	6 M KOH	0.50	5 mV s^{-1}	50
$Ni(OH)_2$/CNTs	Chemical precipitation	432	6 M KOH	0.50	10 mV s^{-1}	51
α-$Ni(OH)_2$/graphene	Chemical precipitation	1215	6 M KOH	0.45	5 mV s^{-1}	27
β-$Ni(OH)_2$/graphene	Hydrothermal	1335	1 M KOH	0.50	2.8 A g^{-1}	17
β-$Ni(OH)_2$	Chemical precipitation	1657	6 M KOH	0.55	2 mV s^{-1}	This work
β-$Ni(OH)_2$/graphene	Chemical precipitation	2194	6 M KOH	0.55	2 mV s^{-1}	This work

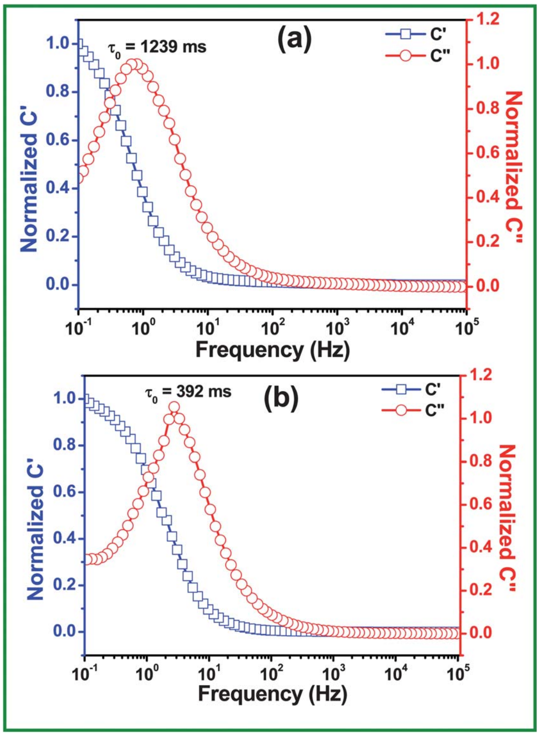

Fig. 7 Normalized real and imaginary part capacitance of (a) pure $Ni(OH)_2$ nanoplates and (b) $Ni(OH)_2$/graphene composite electrodes as a function of frequency. An relatively low relaxation time constant τ_0 (392 ms) was obtained for the $Ni(OH)_2$/graphene electrode, revealing fast accessibility of the electrolyte ions.

part capacitance as a function of frequency (10 mHz to 100 kHz) for each electrode. It can be clearly observed that $C'(\omega)$ gradually decrease with the increase of scan rates for each electrode, however, the $Ni(OH)_2$/graphene composite electrode exhibits slow deterioration of capacitance due to fast ion diffusion and transport (Fig. 7b). In addition, the $C'(\omega)$ of the $Ni(OH)_2$/graphene electrode approaches saturation at a frequency below ~0.2 Hz, which means that equilibrium ion adsorption can be achieved in 5 s, suggesting most of the electrolyte ions reach the adsorption sites.[32] In comparison, the $C'(\omega)$ of $Ni(OH)_2$ electrode does not show any sign of saturation as low as 0.1 Hz, indicating slow diffusion of electrolyte ions owing to the larger particle size and longer diffusion paths. Importantly, the operating frequency (the frequency at which the capacitance $C'(\omega)$ is 50% of its maximum value) of $Ni(OH)_2$/graphene sample is 2.55 Hz, corresponding to the characteristic relaxation time constants τ_0 = 392 ms, which is much lower than that of pure $Ni(OH)_2$ electrode (τ_0 = 1239 ms, Fig. 7), revealing fast accessibility of the electrolyte ions for the $Ni(OH)_2$/graphene sample.[35] The smaller τ_0 of the samples correlates with the better capacitance retention at high scan rates in the CV measurements and accordingly excellent power and energy characteristics.[33] Therefore, $Ni(OH)_2$/graphene composite is a potential promising electrode material for delivering high power and energy.

Since long cycling life is very crucial for high performance supercapacitor electrodes, to test the electrochemical stability, the $Ni(OH)_2$/graphene composite was further tested by repeating CV tests over 2000 cycles at a scan rate of 100 mV s^{-1} in 6 M KOH solution as shown in Fig. 8a. It is worth noting that the specific capacitance increases about 13.7% during the first 80 cycles, which is possibly due to the activation process that increases the number of the available active sites and allows the trapped ions to gradually diffuse out.[36] Importantly, there is only 4.3% capacity deterioration after 2000 continue cycles, much lower than that of the pristine $Ni(OH)_2$ electrode (10.4%), demonstrating the excellent long-term electrochemical stability of the $Ni(OH)_2$/graphene composite. The decay can be probably attributed to the phase transformation or the growth of particle and crystal size of the electrode material during the rapid charge/discharge process in alkali solution.[37]

The ability of the active materials to retain very high specific capacitance at high discharge rates usually contributes to excellent energy and power characteristics. Ragone plots relating the energy density to the power density are an efficient way to evaluate the capacitive performance of supercapacitor electrode materials. The power density and the energy density can be estimated from the following formulas:[38]

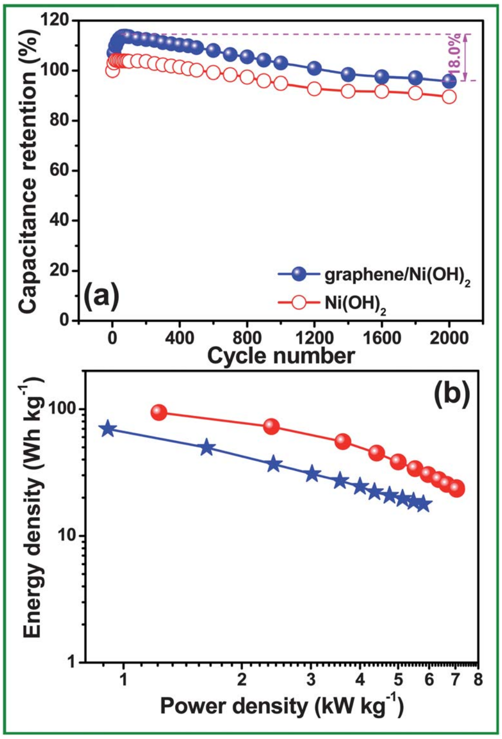

Fig. 8 (a) Long-term cycling performance of the $Ni(OH)_2$/graphene electrode measured at 100 mV s^{-1} in 6 M KOH aqueous solution. (b) Ragone plot of energy density *vs.* power density for $Ni(OH)_2$/graphene electrode.

$$E = \frac{1}{2}C(\Delta V)^2 \tag{7}$$

$$P = \frac{E}{t} \tag{8}$$

where E, C, ΔV, P and t are indicating of the average energy density (Wh kg^{-1}), specific capacitance based on the mass of $Ni(OH)_2$/graphene composite (F g^{-1}), the potential window of discharge (V), average power density (W kg^{-1}) and discharge time (s), respectively. Fig. 8b shows the Ragone polt of the $Ni(OH)_2$/graphene composite derived from the CV curves at different scan rates. Although the specific energy density generally decreases with increase in the specific power density, the $Ni(OH)_2$/graphene electrode exhibits an impressive high specific energy density of 94.0 Wh kg^{-1} at a higher power density of 1.2 kW kg^{-1}. Remarkably, the maximum energy density outperforms that of pure $Ni(OH)_2$ (69.7 Wh kg^{-1}), and is highly comparable to that of the previously reported $Ni(OH)_2$ (52.1 Wh kg^{-1})[39] and $Co(OH)_2$ (80 Wh kg^{-1}).[40] When the power density increases to 7.1 kW kg^{-1}, the energy density drops slowly and can still retain 23.2 Wh kg^{-1}, suggesting that such composite is a highly promising candidate as supercapacitor electrode material for practical applications. For a real symmetric supercapacitor composed of two identical graphene/$Ni(OH)_2$ electrodes, the specific capacitance would be one-fourth of that of a single electrode in a three-electrode cell.[41] In consideration of the specific capacitance of the capacitor charged/discharged in the operating voltage range of 0–0.55 V, a practical energy density of 23.5 Wh kg^{-1} for a symmetric supercapacitor is obtained.

The superhigh specific capacitance, excellent rate capability, superior cycling performance and high energy density of the $Ni(OH)_2$/graphene composite could be attributed to the positive synergistic effect between graphene sheets and $Ni(OH)_2$ nanoparticles. Firstly, nanoscale $Ni(OH)_2$ nanoplates uniformly deposit on the surfaces of graphene sheets, which can not only effectively inhibit the aggregation/restacking of graphene sheets but also significantly improve the kinetics and the electrochemical utilization of $Ni(OH)_2$ due to the extraordinarily shortened ion diffusion and transport length. Secondly, there are numerous mesopores in the $Ni(OH)_2$ nanoplates facilitating the diffusion and transport of electrolyte ions and providing more electrochemical active sites to participate in charge transfer reactions. Thirdly, graphene sheets in the composite could significantly buffer the volume change of $Ni(OH)_2$ and allow the volume expansion to take place easily during the rapid charge/discharge process, which is favorable to obtain better cycling performance. Furthermore, the interconnected nanoflakes of $Ni(OH)_2$ create considerable macropores, which can act as numerous ion-buffering reservoirs offering a robust sustentation of OH^- ions and ensuring that sufficient Faradaic reactions can take place easily at high current densities for energy storage. As a result, this ensures high-rate charge/discharge performance and accordingly high power delivery. Finally, the presence of graphene sheets would contribute the electrical double-layer capacitance to the overall specific capacitance of the electrode due to their inherent high capacitance. All of these features in turn contribute to the superior electrochemical performance of the $Ni(OH)_2$/graphene composite.

4. Conclusions

In conclusion, a simple and scalable method to fabricate hierarchical porous $Ni(OH)_2$ nanoflakes anchored on graphene sheets has been reported. The positive synergistic effect of $Ni(OH)_2$ nanoflakes and graphene sheets results in high energy density, excellent rate capability and good cycle life of the nanocomposite when it is used as a cathode material for aqueous supercapacitors. The composite electrode exhibits the specific capacitance as high as 2194 F g^{-1} at 2 mV s^{-1} in 6 M KOH solution. A maximum energy density of 94.0 Wh kg^{-1} has been obtained. In addition, the electrode exhibits excellent cycling stability with a deterioration of only 4.3% after 2000 cycle tests. It is highly desirable to couple our $Ni(OH)_2$/graphene composite with a promising counter electrode to construct an asymmetric supercapacitor to achieve a wide operating voltage range and further improve the energy and power densities.

Acknowledgements

The authors acknowledge financial support from the National Science Foundation of China (No. 51077014, 21003028), China Postdoctoral Science Foundation (20100480058, 201104411), Heilongjiang Postdoctoral Foundation (LBH-Z10205), Fundamental Research funds for the Central Universities and Program for New Century Excellent Talents in University (NCET-10-0050).

Notes and references

1 P. Simon and Y. Gogotsi, *Nat. Mater.*, 2008, **7**, 845–854.
2 L. H. Bao, J. F. Zang and X. D. Li, *Nano Lett.*, 2011, **11**, 1215–1220.
3 Y. Zhai, Y. Dou, D. Zhao, P. F. Fulvio, R. T. Mayes and S. Dai, *Adv. Mater.*, 2011, **23**, 4828–4850.
4 B. E. Conway, *Electrochemical supercapacitors: Scientific fundamentals and technological applications*, Kluwer Academic/Plenum, New York, 1999.
5 Q. Qu, S. Yang and X. Feng, *Adv. Mater.*, 2011, **23**, 5574–5580.
6 C.-C. Hu, K.-H. Chang, M.-C. Lin and Y.-T. Wu, *Nano Lett.*, 2006, **6**, 2690–2695.
7 H. Wang, Y. Liang, T. Mirfakhrai, Z. Chen, H. S. Casalongue and H. Dai, *Nano Res.*, 2011, **4**, 729–736.
8 R. Lv, T. Cui, M.-S. Jun, Q. Zhang, A. Cao, D. S. Su, Z. Zhang, S.-H. Yoon, J. Miyawaki, I. Mochida and F. Kang, *Adv. Funct. Mater.*, 2011, **21**, 999–1006.
9 J. Li, R. Li, J. M. Wu and H. Su, *J. Power Sources*, 1999, **79**, 86–90.
10 K. W. Jung, D. C. Yang, C. N. Park, C. J. Park and J. Choi, *Int. J. Hydrogen Energy*, 2010, **35**, 13073–13077.
11 S. A. Cheng, W. H. Leng, J. Q. Zhang and C. N. Cao, *J. Power Sources*, 2001, **101**, 248–252.
12 K. Matsui, T. Kyotani and A. Tomita, *Adv. Mater.*, 2002, **14**, 1216–1219.
13 H. Jiang, T. Zhao, C. Z. Li and J. Ma, *J. Mater. Chem.*, 2011, **21**, 3818–3823.
14 Q. H. Huang, X. Y. Wang, J. Li, C. L. Dai, S. Gamboa and P. J. Sebastian, *J. Power Sources*, 2007, **164**, 425–429.
15 S. M. Bak, K. H. Kim, C. W. Lee and K. B. Kim, *J. Mater. Chem.*, 2011, **21**, 1984–1990.
16 J. Zhang, L. B. Kong, J. J. Cai, H. Li, Y. C. Luo and L. Kang, *Microporous Mesoporous Mater.*, 2010, **132**, 154–162.
17 H. Wang, H. S. Casalongue, Y. Liang and H. Dai, *J. Am. Chem. Soc.*, 2010, **132**, 7472–7477.
18 S. Park and R. S. Ruoff, *Nat. Nanotechnol.*, 2009, **4**, 217–224.
19 C. G. Liu, Z. N. Yu, D. Neff, A. Zhamu and B. Z. Jang, *Nano Lett.*, 2010, **10**, 4863–4868.
20 Z. Fan, J. Yan, L. Zhi, Q. Zhang, T. Wei, J. Feng, M. Zhang, W. Qian and F. Wei, *Adv. Mater.*, 2010, **22**, 3723–3728.
21 J. Yan, T. Wei, B. Shao, Z. J. Fan, W. Z. Qian, M. L. Zhang and F. Wei, *Carbon*, 2010, **48**, 487–493.
22 Y. W. Zhu, M. D. Stoller, W. W. Cai, A. Velamakanni, R. D. Piner, D. Chen and R. S. Ruoff, *ACS Nano*, 2010, **4**, 1227–1233.
23 A. V. Murugan, T. Muraliganth and A. Manthiram, *Chem. Mater.*, 2009, **21**, 5004–5006.
24 B. J. Li, H. Q. Cao, J. Shao, H. Zheng, Y. X. Lu, J. F. Yin and M. Z. Qu, *Chem. Commun.*, 2011, **47**, 3159–3161.
25 F. Tuinstra, *J. Chem. Phys.*, 1970, **53**, 1126–1130.
26 S. R. Shieh and T. S. Duffy, *Phys. Rev. B*, 2002, **66**, 134301–134308.
27 J. W. Lee, T. Ahn, D. Soundararajan, J. M. Ko and J.-D. Kim, *Chem. Commun.*, 2011, **47**, 6305–6307.
28 D. W. Wang, F. Li, M. Liu, G. Q. Lu and H. M. Cheng, *Angew. Chem., Int. Ed.*, 2008, **47**, 373–376.
29 T. I. Lee, J. P. Jeagal, J. H. Choi, W. J. Choi, M. J. Lee, J. Y. Oh, K. B. Kim, H. K. Baik, Y. Xia and J. M. Myoung, *Adv. Mater.*, 2011, **23**, 4711–4715.
30 H. Gomez, M. K. Ram, F. Alvi, P. Villalba, E. Stefanakos and A. Kumar, *J. Power Sources*, 2011, **196**, 4102–4108.
31 A. J. Bard and L. R. Faulkner, *Electrochemical methods: fundamentals and applications*, John Wiley & Sons, New York, 2001.
32 Y. Korenblit, M. Rose, E. Kockrick, L. Borchardt, A. Kvit, S. Kaskel and G. Yushin, *ACS Nano*, 2010, **4**, 1337–1344.
33 L. Wei, M. Sevilla, A. B. Fuertes, R. Mokaya and G. Yushin, *Adv. Energy Mater.*, 2011, **1**, 356–361.
34 V. Ganesh, S. Pitchumani and V. Lakshminarayanan, *J. Power Sources*, 2006, **158**, 1523–1532.
35 D. Pech, M. Brunet, H. Durou, P. H. Huang, V. Mochalin, Y. Gogotsi, P. L. Taberna and P. Simon, *Nat. Nanotechnol.*, 2010, **5**, 651–654.
36 X. J. Zhang, W. H. Shi, J. X. Zhu, W. Y. Zhao, J. Ma, S. Mhaisalkar, T. L. Maria, Y. H. Yang, H. Zhang, H. H. Hng and Q. Y. Yan, *Nano Res.*, 2010, **3**, 643–652.
37 G. X. Hu, C. X. Li and H. Gong, *J. Power Sources*, 2010, **195**, 6977–6981.
38 Z. Fan, J. Yan, T. Wei, L. Zhi, G. Ning, T. Li and F. Wei, *Adv. Funct. Mater.*, 2011, **21**, 2366–2375.
39 D. S. Kong, J. M. Wang, H. B. Shao, J. Q. Zhang and C. N. Cao, *J. Alloys Compd.*, 2011, **509**, 5611–5616.
40 X. Xia, J. Tu, Y. Zhang, Y. Mai, X. Wang, C. Gu and X. Zhao, *J. Phys. Chem. C*, 2011, **115**, 22662–22668.
41 J. Yan, J. Liu, Z. Fan, T. Wei and L. Zhang, *Carbon*, 2012, **50**, 2179–2188.
42 J. W. Lee, J. M. Ko and J. D. Kun, *J. Phys. Chem. C*, 2011, **115**, 19445–19454.
43 M.-S. Wu and K.-C. Huang, *Chem. Commun.*, 2011, **47**, 12122–12124.
44 Y.-x. Wang, Z.-a. Hu and H.-y. Wu, *Mater. Chem. Phys.*, 2011, **126**, 580–583.
45 M. Aghazadeh, A. N. Golikand and M. Ghaemi, *Int. J. Hydrogen Energy*, 2011, **36**, 8674–8679.
46 Z. Y. Lu, Z. Chang, W. Zhu and X. M. Sun, *Chem. Commun.*, 2011, **47**, 9651–9653.
47 Y. F. Yuan, X. H. Xia, J. B. Wu, J. L. Yang, Y. B. Chen and S. Y. Guo, *Electrochim. Acta*, 2011, **56**, 2627–2632.
48 U. M. Patil, K. V. Gurav, V. J. Fulari, C. D. Lokhande and O. S. Joo, *J. Power Sources*, 2009, **188**, 338–342.
49 J. P. Liu, C. W. Cheng, W. W. Zhou, H. X. Li and H. J. Fan, *Chem. Commun.*, 2011, **47**, 3436–3438.
50 S. Chen, J. W. Zhu, H. Zhou and X. Wang, *RSC Adv.*, 2011, **1**, 484–489.
51 C.-G. Liu, Y.-S. Lee, Y.-J. Kim, I.-C. Song and J.-H. Kim, *Synth. Met.*, 2009, **159**, 2009–2012.